Numerical Simulation of Flow and Heat Transfer Characteristics of a Liquid Jet Impinging on a Cylindrical Cavity Heat Sink

Z. G. Tang, F. Deng, S. C. Wang and J. P. Cheng[†]

School of Mechanical Engineering, Hefei University of Technology, Hefei, Anhui, 230009, China

†*Corresponding Author Email: chjianping@hfut.edu.cn*

ABSTRACT

In this study, the flow and heat transfer characteristics of a liquid jet impinging on cylindrical cavity heat sinks with a local body heat source were numerically investigated. The Transition SST turbulence model was validated and adopted. The parameters of structure and flow, including d/D = 2, 3, and 4, h/D = 0.05, 0.10, 0.15, and 0.20, and Re = 5,000, 10,000, and 23,000, were investigated. The results revealed that the adoption of a cylindrical cavity structure can improve the heat transfer capacity of the heat sink. A horseshoe vortex introduced by an inclined jet near the cavity edge region improved the heat transfer performance. The maximum enhancement of the cylindrical cavity heat sink was 11.8% compared with the flat plate heat sink when d/D = 3, h/D = 0.15, and Re = 23,000.

Keywords: Liquid impingement; Cylindrical cavity heat sink; Horseshoe vortex; Numerical simulation.

NOMENCLATURE

D	nozzle diameter	Nu_x	local Nusselt number
D_{heat}	heat source diameter	Re	Reynolds number
D_{plate}	heat sink diameter	u_0	inlet velocity
d	cylindrical cavity diameter		
H	nozzle-to-plate distance	ΔH	nozzle length
h	cylindrical cavity length	δ	heat sink thickness
Nu_{ave}	average Nusselt number	δ_{heat}	heat source thickness

1. INTRODUCTION

With the advancement of technology and the needs of products, electronic components are developing toward high integration, miniaturization and high energy consumption. Meanwhile, the problem of rising heat flux density is becoming increasingly more significant, and a series of enhanced heat transfer technologies and heat sinks have been developed to address this issue. Among them, the impinging jet has been greatly valued by researchers due to its extremely high heat and mass transfer rates, and the convenient adjustment of the system.

Research on impinging jets was conducted as early as 1977, when Martin (1977) researched several factors affecting the heat and mass transfer between impinging air jets and solid surfaces, including the turbulence properties, the target surface parameters, and the angle of impact, and derived the correlation of the impinging jet for engineering applications by summarizing numerous works of existing literature. Buchlin (2011) investigated the heat transfer by convection of single and multiple jet systems. Experimental data obtained from infrared thermography are compared to CFD simulations. He pointed out the effect of the jet tilting, thermal entrainment and jet confinement in particular. Chandramohan *et al*. (2016) investigated the variation in temperature, heat transfer coefficient and Nusselt number of a hot plate subjected to multi-jet air impingement cooling. They found that significant contributions on outputs are due to the effect of H/D ratio and Reynolds number.

The heat sink, an important component of the impinging jet, is one of the factors that enhances the

heat transfer effect of the jet. Different structures of heat sinks have been investigated for optimal heat transfer performance, including the plate/pin-fin heat sink, micro-channel heat sink, porous medium heat sink, protruding pedestal heat sink, and cavity heat sink.

Wong and Indran (2013) numerically investigated the effects of variable channel and inlet widths both with and without fillet profiles on the flow and heat transfer characteristics of plate-fin heat sinks. The results showed that the thermal performance could be enhanced by fillet profiles. Abouali and Baghernezhad (2010) employed rectangular and arc groove shapes to enhance the heat removal rate for single-phase cooling in micro pin-fin heat sinks. They numerically investigated the pressure drop and heat transfer characteristics of single-phase micro pin-fin heat sinks for laminar flow, and found that the grooved micro-channels had higher heat removal rates than the simple micro-channel. Zhao *et al*. (2016) numerically investigated the flow and heat transfer characteristics of a micro square pin-fin heat sink, and compared them with the characteristics of a micro column pin-fin heat sink. The results indicated that the micro square pin-fin heat sink presented better thermal performance than micro column pin-fin heat sink when the porosity and located angle were 0.75 and 30°, respectively.

Tuckermann and Pease (1981) first designed a micro-channel heat sink that cooled silicon-integrated circuits with a heat flux of 790 W/cm^2. Huang *et al*. (2017) applied the field synergy principle and numerically simulated the heat transfer characteristics of a micro-channel heat sink with and without different dimple structures. The results revealed that the micro-channel heat sink with convex dimples exhibited the best overall performance. Robinson *et al*. (2018) designed a micro-channel jet heat sink using the MICA Freeform process. When the flow rate was 0.5 L/min, the effective heat transfer coefficient was found to reach 400 kW/ (m^2 • K), and the heat sink could therefore be used to cool electronic components with the target heat flux density of 1 kW/cm^2.

Chan (2015) experimentally investigated the heat transfer characteristics of an aluminum foam heat sink subjected to an impinging air jet. He found that when the Reynolds number was low, the thermal performance of the foam heat sink was better than that of a pin-fin heat sink with the same porosity, and the trend was reversed for larger Reynolds numbers. Kumar and Pattamatta (2017) experimentally investigated the convective heat transfer performance in jet impingement cooling using various porous media configurations via the liquid crystal thermography technique. They discovered maximum enhancements in the average Nusselt number by 52.71% and 74.68%, and the Nusselt number in the stagnation region by 58.08% and 53.80% when the Reynolds number was 400 and 700, respectively.

In the current study, the structures of the jet impinging on the protruding pedestal include square, spherical, and conical structures. Fleischer and Nejad (2004) investigated the effect of a square protruding pedestal on impinging jets. They found that the average heat transfer was increased by 5%-15% compared to that of a flat surface. Additionally, when the Reynolds number was low and the jet diameter was large, the flow separation and reattachment at the edge of the pedestal were found to be large. Zhang *et al*. (2013) studied a single jet impinging on a spherical protruding surface. They concluded that both heat transfer enhancement within the stagnation region and the increase of the heat transfer area led to the overall heat transfer improvement of the jet impinging on a protruding target surface. Tang *et al*. (2017) proposed the use of a jet array cooling cone heat sink, and analyzed the influence of parameters including the cone angle, nozzle diameter, jet Reynolds number, and heat flux density on the average heat transfer performance of the cone heat sink. The results showed that the heat transfer performance of the cone heat sink was superior to that of a flat plate heat sink.

The research on the heat transfer enhancement technology of jet impingement on a cavity is currently concentrated on spherical cavities. Terekhov *et al*. (2009) measured the distributions of flow velocities, the fields of pressure and the heat-transfer coefficients inside the cavity, and found that, at a certain depth, the cavity generates a large-scale toroidal vortex, essentially influencing the heat transfer. Xie *et al*. (2013) numerically investigated the flow and heat transfer characteristics of a single jet impinging on a dimpled surface. They found that the range of the Nusselt stagnation area expanded with the increase of the depth, and obtained the correlative expressions of the local Nusselt number, the Nusselt number in stagnation points, and the average Nusselt number.

In recent decades, the cylindrical cavity structure for jet impinging has also gained attention. Shuja *et al*. (2005; 2007; 2009) and Yilbas *et al*. (2009) studied the influence of the nozzle cone angle, the diameter and depth of the cavity, and the jet velocity on the flow and heat transfer characteristics of an air jet impinging on a cylindrical cavity heat sink with a surface heat source. The results showed that increasing the cavity diameter and jet velocity significantly changed the fluid flow structure, and that the heat transfer rate was affected by the nozzle cone angle, the jet velocity, and the diameter and depth of the cavity. In their research, an air jet was adopted, wherefore the effective flow and heat transfer area of the jet were limited due to the characteristics of the gas; additionally, a constant temperature boundary and uniform heat flux boundary were utilized, and no other types of heat source were considered.

In summary, heat sinks of different structures can enhance the heat transfer capacity to varying degrees. At present, researchers have systematically studied the heat sinks of most structures, but less research has been conducted on the cylindrical cavity heat sink. Therefore, in this paper, the flow
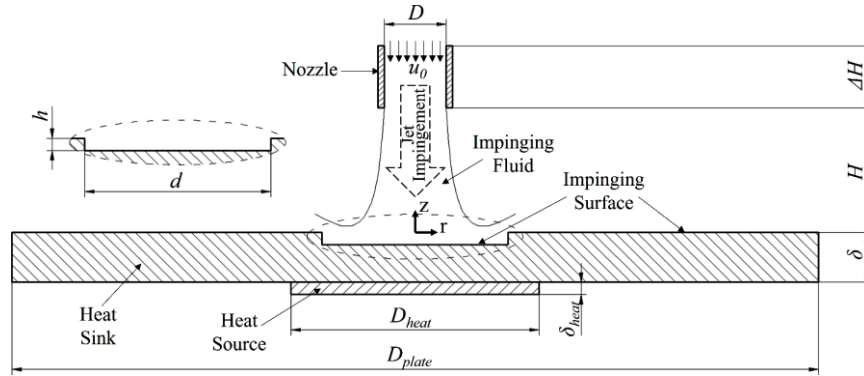
Fig. 1. Schematic of a section for jet impinging on a cylindrical cavity heat sink.

and heat transfer characteristics of liquid impinging on the cylindrical cavity heat sink with a local body heat source are analyzed from the perspective of fluid flow with the comprehensive consideration of various factors, and the heat transfer performance of the heat sink is evaluated from many aspects.

2. PHYSICAL MODEL AND NUMERICAL METHOD

2.1 Physical Model

The section of a physical model for a single liquid jet impingement cooling system is illustrated in Fig. 1. The coolant (water) throughout a circular nozzle impinged on a cylindrical cavity heat sink, and aluminum was selected as the material for the entire heat sink. A simplified chip structure considered as a local body heat source was placed in the middle of the bottom of the heat sink. Other sizes of the jet system are also identified in Fig. 1. The simplified nozzle was 10 mm in diameter (D) and 10 mm in length (ΔH). The heat sink had a diameter (D_{plate}) of 130 mm and a thickness (δ) of 8 mm. At the top of the heat sink was a cylindrical cavity. The distance (H) from the nozzle to the upper surface of the heat sink was 20 mm. The jet Reynolds number (Re), the diameter ratio (d/D), and relative depth (h/D) of the cylindrical cavity were used as variables in this work. These parameters are listed in Table 1.

Table 1 Main geometry of a single jet impingement cooling system

Parameters	Values
Reynolds number (Re)	5000, 10,000, 23,000
Diameter ratio (d/D)	2, 3, 4
Relative depth (h/D)	0.05, 0.10, 0.15, 0.20

2.2 Governing Equations and Parameter Definitions

In this study, the maximum velocity was less than 3 m/s for each case. The fluid flow was considered to be incompressible, steady, and axisymmetric. The VOF formulation was adopted to solve the water and air interface, and radiation dissipation and gravity were ignored. By employing these approximations, the associated governing equations were established as follows.

Volume fraction equation:

$$v_i \cdot \nabla \alpha_i = 0 \tag{1}$$

Continuity equation:

$$\nabla \cdot (\rho_{eff} V) = 0 \tag{2}$$

Momentum equation:

$$\nabla \cdot (\rho_{eff} VV) = \rho_{eff} \cdot F - \nabla p + \nabla \cdot (\mu_{eff} \nabla V) \tag{3}$$

Energy equation for fluid:

$$\nabla \cdot [\vec{w}(\rho_{eff} E)] = \nabla \cdot (k_{eff} \nabla T_f) \tag{4}$$

where,

$$E = \frac{\sum_{i=1}^{n} \alpha_i \rho_i E_i}{\sum_{i=1}^{n} \alpha_i \rho_i} \tag{5}$$

Energy equation for solid:

$$\nabla \cdot (k_s \nabla T_s) = 0 \tag{6}$$

The density, viscosity, and thermal conductivity are respectively given by the following equations:

$$\rho = \alpha_i \rho_f + (1 - \alpha_i) \rho_{air} \tag{7}$$

$$\mu = \alpha_i \mu_f + (1 - \alpha_i) \mu_{air} \tag{8}$$

$$k = \alpha_i k_f + (1 - \alpha_i) k_{air} \tag{9}$$

The governing equations were solved by a CFD solver, FLUENT. The RANS method was employed to solve the Reynolds stress. The convection term was discretized by the second-order upwind interpolation scheme. The coupling between pressure and velocity was handled by the SIMPLE algorithm. The residuals were less than 10^{-5}. The parameters for the evaluation of numerical results are defined below.

Jet Reynolds number:

$$Re = \frac{\rho_f u_0 D}{\mu_f} \tag{10}$$

where D is the inner diameter of the nozzle, u_0 is the mean velocity of the nozzle exit, ρ_f and μ_f are the density and dynamic viscosity of water, correspondingly.

Local Nusselt number:

$$Nu_x = \frac{qD}{(T_{w,x} - T_f)k_f} \quad (11)$$

where q, $T_{w,x}$, T_f, and k_f are respectively the heat flux, temperatures of the wall and fluid, and thermal conductivity of water.

Average Nusselt number:

$$Nu_{ave} = \frac{\Sigma Nu_{x,i} dA_i}{\Sigma dA_i} \quad (12)$$

where $Nu_{x,i}$ is the local Nusselt number for each discretized element, and dA_i is the area of each impinged element.

2.3 Turbulence Modeling Validation

The selection of turbulence models is difficult for the accuracy of the calculation results, although many turbulence models are currently provided in FLUENT. Each turbulence model possesses its own application scope and limitation. The commonly used turbulence models which were considered for initial comparison with the relevant experimental results were the Realizable k-ε model (Elebiary and Taslim 2011), v^2-f model (Bhagwat and Sridharan 2016), SST k-ω model (Yang *et al.* 2014), and Transition SST model (Zhang *et al.* 2013). The verification model used was a single impingement jet with detailed experimental data of heat transfer characteristics. The main parameters and boundary conditions of the numerical simulation were the same as those used in the experiments (Baughn and Shimizu 1989; Baughn *et al.* 1991; Yan *et al.* 1992).
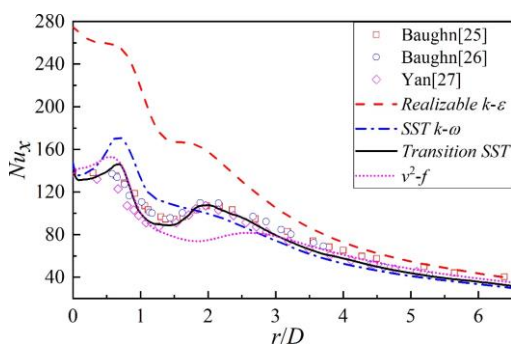
Fig. 2. Comparison of the local Nusselt numbers between different turbulence models and experimental results.

The experimental and numerical data are presented in Fig. 2. The v^2-f, SST k-ω, and Transition SST models agreed well with the experimental data, though the Realizable k-ε model did not. The curve of the v^2-f model increased when $1.5 < r/D < 2.5$. The low local Nusselt numbers were shown to be in the stagnation region for the v^2-f and SST k-ω models. Thus, the Transition SST model was

adopted to solve the momentum equation. The curves of the Transition SST model agreed well with the conical experimental data. The numerical results were slightly low, but the trend of the local Nusselt numbers were revealed to be in the stagnation region. The transport equations for the Transition SST model are listed below:

$$\rho \frac{\partial}{\partial x_i}(u_i \gamma) = P_{\gamma_1} - E_{\gamma_1} + P_{\gamma_2} - E_{\gamma_2} + \frac{\partial}{\partial x_i}\left(\mu \frac{\partial \gamma}{\partial x_i}\right) \quad (13)$$

$$\rho \frac{\partial}{\partial x_i}(u_i Re_\theta) = P_\theta + \frac{\partial}{\partial x_i}\left(\sigma_\theta \mu \frac{\partial Re_\theta}{\partial x_i}\right) \quad (14)$$

where $P_{\gamma 1}$ and $E_{\gamma 1}$ are the transition sources, $P_{\gamma 2}$ and $E_{\gamma 2}$ are the destruction sources, and P_θ is the source term for transition momentum thickness Reynolds number.

2.4 Boundary Conditions and Grid Details

The computational domain contained both fluid and solid domains. The three-dimensional geometric model was simplified to a two-dimensional model, and one-half of the two-dimensional geometric model was regarded as the entire computational domain in accordance with the assumption of axisymmetric flow in Section 2.2. At the nozzle inlet, the flow was fully turbulent with a turbulence intensity of 4.1%, and the fluid temperature was 300 K. The pressure outlet was the atmosphere. The impinged surface, which is the coupling surface of fluid and solid, was non-slip, and its initial temperature was 300 K. The axis boundary conditions were utilized on the fluid/solid symmetric centerline. A constant heating power of 200 W/cm^3 was applied to the simplified chip heat source. Other solid surfaces were adiabatic walls.

The 2D computational grid is illustrated in Fig. 3. The structured grid, generated by ANSYS ICEM software, was adopted to obtain results with appropriate accuracy and efficient computation. The refined grid was carried out in the entire heat sink and the region of water flow. The Y+ per case was less than 1.0.

A grid sensitivity test was performed to ensure grid independence for numerical simulations. The main parameters were $Re = 10{,}000$, $d/D = 3$, and $h/D = 0.10$. Four grid sizes were designed to discretize the computational domain. Table 2 lists the predicted average Nusselt number (Nu_{ave}) and the center point temperature (T_{sta}) of the cylindrical cavity. The deviation between Grid 3 and 4 is the smallest; thus, the design of Grid 3 was adopted for all cases considering the amount of calculation.

3. RESULTS AND DISCUSSION

This section exhibits the numerical results of the flow and heat transfer for a water jet impinging on a cylindrical cavity, and the results are discussed. The investigated variables were the jet Reynolds number ($Re = 5000$, $10{,}000$, and $23{,}000$), the diameter ratio ($d/D = 2$, 3, and 4), and the relative depth ($h/D = 0.05$, 0.10, 0.15, and 0.20) of the cylindrical cavity.

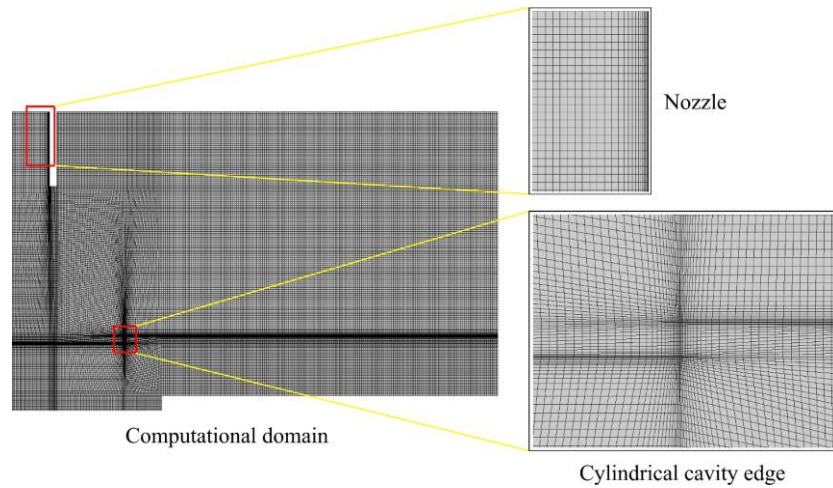**Fig. 3. Details of grid design on boundary layer.**

Table 2 Grid independence test results

		Grid 1	Grid 2	Grid 3	Grid 4
Grid number		35,026	42,812	51,952	63,034
Nu_{ave}	Value	81.14	83.01	84.36	83.82
	Deviation/%	-2.30	-1.63	0.64	-
T_{sta}	Value/k	322.2	322.9	323.3	323.1
	Deviation/%	-0.22	-0.12	0.06	-

Flat plate heat sink   Cylindrical cavity heat sink
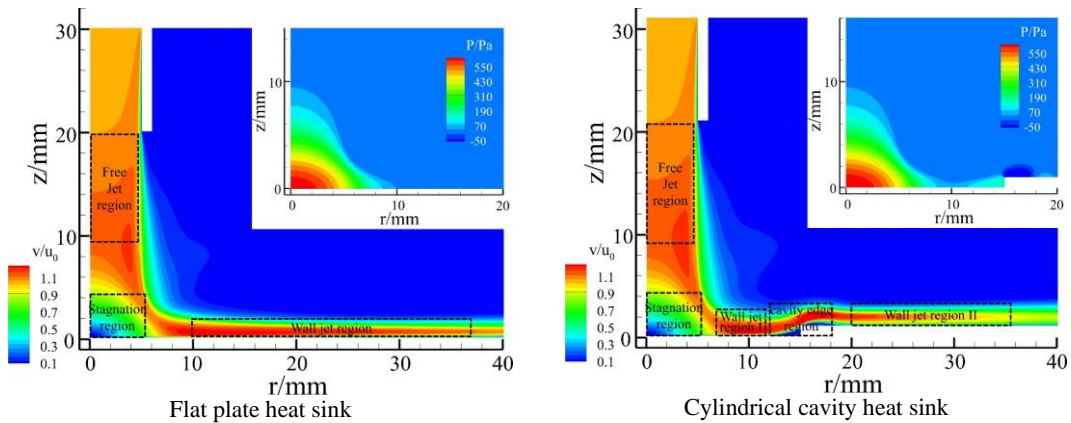
Fig. 4. Contours of velocity and static pressure.

The fluid flow was evaluated with contours of velocity and static pressure, and the streamline distribution of the jet area. The heat transfer study included the temperatures of the heat sinks, distributions of the local Nusselt numbers, and the average Nusselt numbers.

3.1 Flow Characteristics

The contours of velocity and local static pressure for the jet impinging on a flat plate heat sink (Re = 10,000) and a cylindrical cavity heat sink (Re = 10,000, d/D = 3, and h/D = 0.10) are demonstrated in Fig. 4. The axial and radial directions are presented with the coordinates z and r, respectively. Dimensionless velocity, which is the ratio of local velocity to inlet velocity, was adopted.

The jet flow velocity was accelerated after punching out the nozzle. In the free jet region, the maximum

ratio of the velocity of the jet impinging on the flat plate was 1.16, and that of the jet impinging on the cylindrical cavity was 1.17. As the jet impinged on the stagnation region, the axial velocity of the jet was greatly reduced due to the obstruction of the plate, the fluid was forced to flow to both sides, and the radial velocity was increased, as presented in Fig. 5. A local high-pressure zone was observed in the stagnation region. On the flat plate heat sink, the velocity recovered after the fluid broke away from the stagnation region, and reached the level of the free jet region. The fluid continued to flow along the wall, and the static pressure on the wall was small. However, on the cylindrical cavity heat sink, fluid flowed along the bottom surface and continued to impact the sidewall of the cavity after breaking away from the stagnation region. Next, the fluid leapt out of the cavity and then hit the plate again after reaching a certain height, and a local negative

727

pressure zone was observed in this area. In accordance with the characteristics of velocities and pressure distributions, the near-wall flow area of the cylindrical cavity heat sink was divided into four regions, namely the stagnation region, wall jet region I, cavity edge region, and wall jet region II, as shown in Fig. 4(b).

The stagnation region existed in an area where the range of r/D was less than 0.6. As it approached the bottom of the cavity, the axial velocity decreased sharply, while the radial velocity gradually increased. The fluid was forced to flow to both sides due to the obstruction of the plate, and a local high pressure zone was formed. The larger the jet Reynolds number, the greater the pressure in the high-pressure zone due to the greater fluid impact. For different heat sink structures (different values of d/D and h/D), the distributions of velocity and static pressure of the jet flow in the stagnation region were nearly identical, as shown in Figs. 6 and 7.
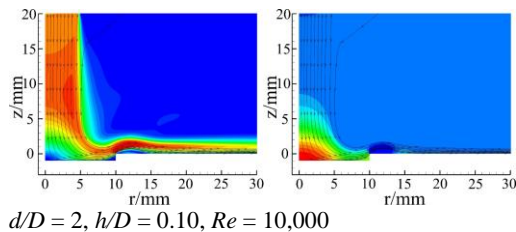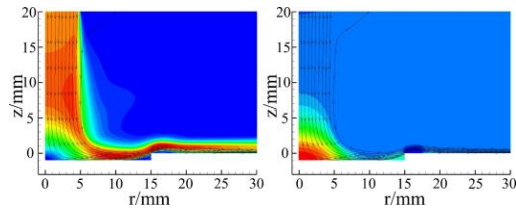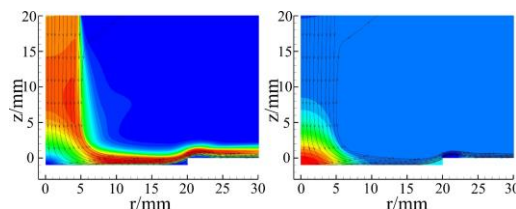

axial velocity   radial velocity
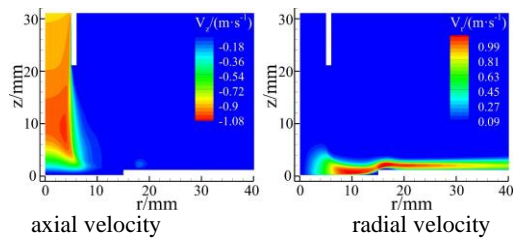
Fig. 5. Distribution of the velocity of a cylindrical cavity heat sink.
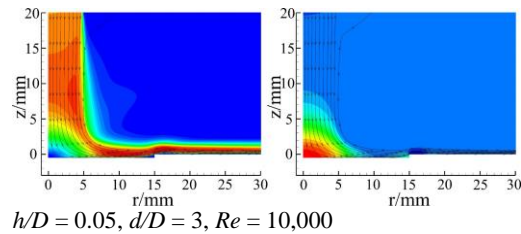

$d/D = 2$, $h/D = 0.10$, $Re = 10,000$

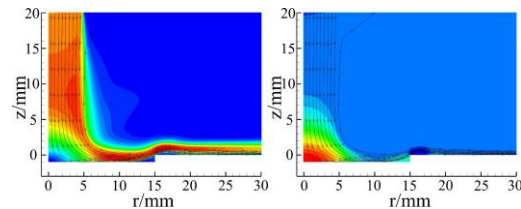
$d/D = 3$, $h/D = 0.10$, $Re = 10,000$

$d/D = 4$, $h/D = 0.10$, $Re = 10,000$

Fig. 6. Velocity contour (left), static pressure contour (right) and streamlines at different cavity diameters.

There was a short wall jet region I before the jet flow exited the stagnation region to the edge of the cavity. The radial velocity increased rapidly and eventually reached the maximum velocity of the free jet region. The static pressure gradually tended to 0 when $d/D = 3$ and 4. When $d/D = 2$, the wall jet region I was almost non-existent due to the too-small diameter of the cavity. Additionally, the larger the value of d/D, the longer the wall jet region I.
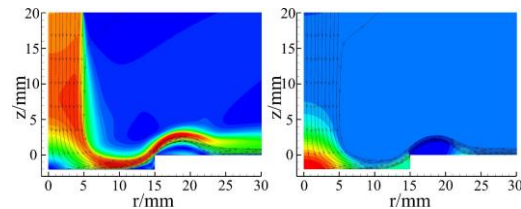

$h/D = 0.05$, $d/D = 3$, $Re = 10,000$

$h/D = 0.10$, $d/D = 3$, $Re = 10,000$
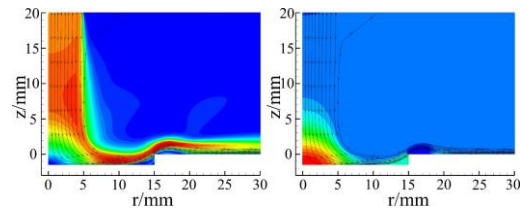
$h/D = 0.15$, $d/D = 3$, $Re = 10,000$

$h/D = 0.2$, $d/D = 3$, $Re = 10,000$

Fig. 7. Velocity contour (left), static pressure contour (right) and streamlines at different cavity depths.

The jet flow reached the cavity edge region after the short wall jet region I. The velocities and pressure changed dramatically, and two vortexes appeared here. The radial velocity of the upper fluid was reduced to a small level, and then restored to its previous level. The radial velocity of the underlying fluid in the cavity rapidly decreased to zero and then became negative, creating a vortex. When the fluid leapt out of the cavity, the axial velocity was negative, the rate first increased and then decreased, and when the fluid rose to the highest point, the velocity became 0. Then, when the fluid fell again against the plane, the axial velocity was positive; it

first increased and then decreased to 0. The radial velocity of the bottom layer of the fluid after leaping out of the cavity changed from positive to negative, and a vortex formed again. Additionally, a local negative pressure region was formed here. When d/D increased, the negative pressure zone decreased slightly; when h/D increased, the negative pressure zone increased obviously.

When the fluid leapt out of the cavity and impacted the plate again, as shown in Fig. 8, the velocity near the wall was small, the local pressure on the wall was high, and the streamlines were separated to both sides. These characteristics are similar to those of the stagnation region when a jet impinges on a flat plate. Thus, this zone is also called the secondary stagnation region, and the impinging flow is called the secondary jet, which is an inclined jet. The fluid on the left of the secondary zone upward along the wall flowed opposite to the mainstream direction, and the velocity increased over the secondary stagnation zone. The high-velocity fluid for the secondary impingement was a result of upstream flow separation. The flow separation, secondary jet, and wall confinement induced a horseshoe vortex in accordance with its cause. When d/D increased, the local high pressure region decreased; and when h/D increases, the local high pressure region increased.
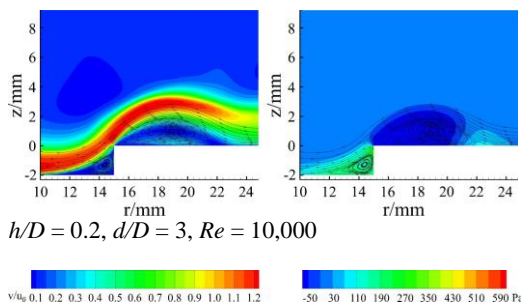

$h/D = 0.2$, $d/D = 3$, $Re = 10,000$

Fig. 8. Velocity contour (left), static pressure contour (right) and streamlines in the cavity edge region.

The jet then flowed into the wall jet region II. The axial velocity disappeared, and the static pressure dropped to 0. In addition, due to the friction of the plane and the viscosity of the fluid, the radial velocity gradually decreased and tended to be smooth. However, the recovery of the radial velocity was worse when h/D was increased.

3.2 Heat Transfer Characteristics

The temperature distributions of cylindrical cavity heat sinks with different typical structures are presented in Fig. 9. Because the body heat source was located at the center of the bottom of the heat sink and was small in volume, the high temperature was concentrated in the center area. The temperature in the heat sink area away from the heat source decreased rapidly. As is evident from the temperature distribution diagram, the partial cavity structures had significant cooling effects compared with the flat plate heat sink. Additional heat transfer details are difficult to obtain from the temperature

distributions of heat sinks; thus, the Nusselt number was used to evaluate their thermal performances.

The local Nusselt numbers of different parameters are presented in Fig. 10. Overall, the local Nusselt number decreased as r/D increased. Figures 10(a), 10(b), and 10(c) respectively present the effect of different Reynolds numbers and different values of d/D and h/D on the distributions of local Nusselt numbers.

In the stagnation region, the local Nusselt number was in a higher level. Because the bottom of the cylindrical cavity was a plane, the distribution of the local Nusselt number of the cylindrical cavity heat sink in the stagnation region was almost identical to that of the flat plate heat sink. It is noted that the local Nusselt number first decreased slightly and then increased with the increase of r/D. Its maximum value was 19.1% higher than that of the stagnation point. The distributions of local Nusselt numbers with different cavity structures were similar. However, overall, the higher the Reynolds numbers, the higher the local Nusselt numbers. Unlike when $Re = 5,000$ and $10,000$, when $Re = 23,000$, the local Nusselt number decreased slightly after increasing.

In the wall jet region I, as r/D increased, the Nusselt number decreased sharply as the fluid impacted the sidewall of the cavity and the radial velocity decreased dramatically. The higher the Reynolds number and the larger the value of h/D, the faster the decrease of the local Nusselt number. A larger d/D indicates a longer wall jet region I, and the slower decline of the local Nusselt number.

In the cavity edge region, the complex flow structure caused the local Nusselt number curve to fluctuate greatly, and the local Nusselt number here presented three peaks. The impact of the fluid on the sidewall of the cavity caused the near-wall surface Nusselt number to increase rapidly and form the first peak, which is similar to the vertical impact of the jet from the nozzle. The fluid then reached the edge of the cavity, and the flow boundary layer here was rapidly thickened; thus, the heat transfer was seriously deteriorated, and the local Nusselt number was decreased. Its minimum was less than 13 for the structure of $d/D = 3$, $h/D = 0.10$. The fluid leapt out and impacted the top of the sidewall, and the flow boundary layer here became thin; thus, the local Nusselt number increased again to form the second peak. The fluid then fell and impacted the plate again, and a horseshoe vortex was formed here. In general, the horseshoe vortex first weakened the heat transfer, and then strengthened it. Therefore, after reaching the second peak, the local Nusselt number first decreased and then increased to finally reach the third peak. The mechanism of heat transfer enhancement was the same as that of the stagnation region with a slanted jet impacted on the plate. As the d/D increased, the heat transfer enhancement performance of the horseshoe vortex weakened. The area of the horseshoe vortex clearly expanded toward the edge of the plate when $h/D = 0.20$, and its heat transfer enhancement performance was slightly weakened.
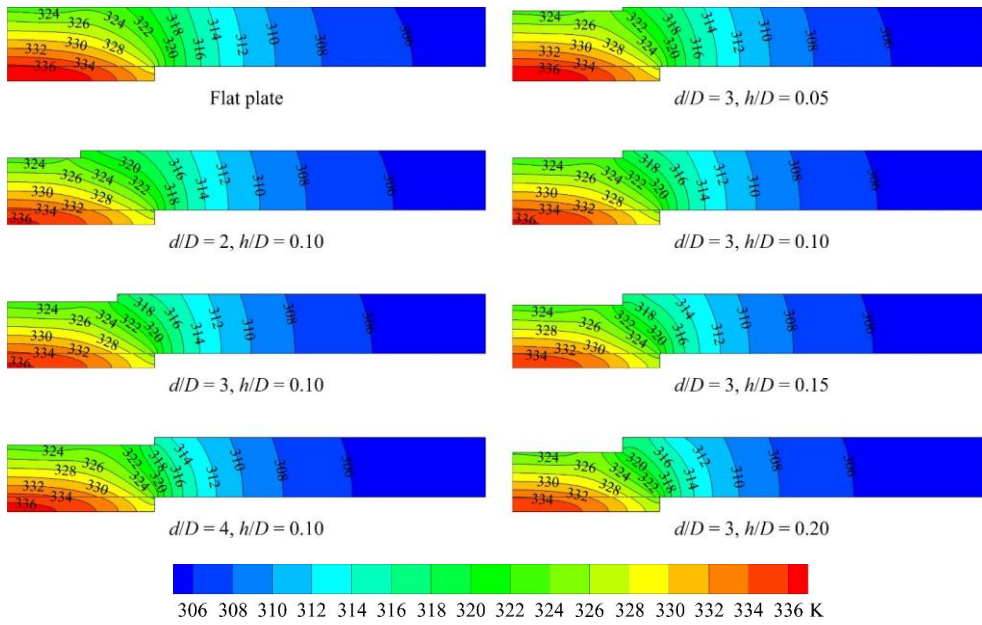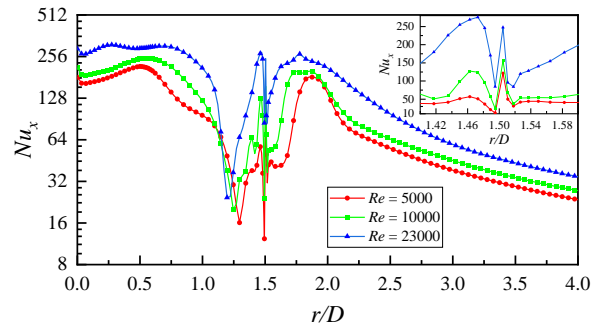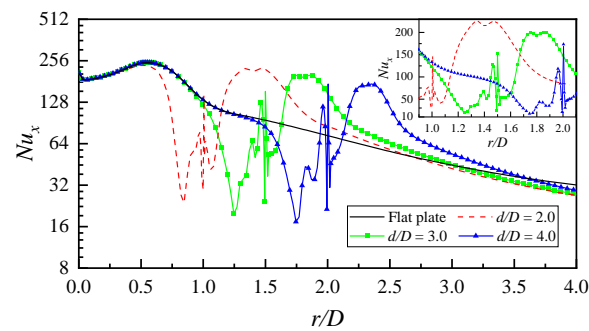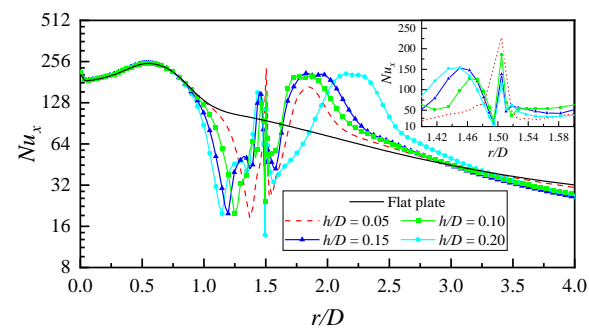
Fig. 9. Distributions of temperatures of heat sinks, *Re* =10,000.

Different *Re*, *d/D* = 3, *h/D* = 0.10

Different *d/D*, *h/D* = 0.10, *Re* = 10,000

Different *h/D*, *d/D* = 3, *Re* = 10,000

Fig. 10. Distributions of the local Nusselt numbers.

In the wall jet region II, the local Nusselt number continued to decrease with the increase of *r/D*. Additionally, the local Nusselt number curves under different structures, including the flat plate, gradually coincided. However, the Nusselt numbers of the cavity structure were all lower than those of the flat plate. This is because the fluid spread out on the plate, the flow was gentle, and the structure was single; however, the velocity of flow in the cavity structure was lower. This also demonstrates that the upstream flow and heat transfer differences have less influence on this region.

The heat transfer difference between different conditions was well studied from the radial distribution of the local Nusselt numbers, which are difficult to be used to directly and accurately summarize the overall heat transfer capacity of the heat sink. Thus, the average Nusselt number was introduced to evaluate the overall heat transfer of the heat sinks. The average Nusselt number is defined by Eq. (12). The range of *r/D* from 0-4 was examined, and the average Nusselt numbers are listed in Fig. 11. In the figure, the average Nusselt number of the plate heat sink was taken as the reference for that of different cavity structures at different Reynolds numbers. When *Re* = 5,000 and 10,000, the average Nusselt numbers of various cavity diameters at *h/D* = 0.05 and various cavity depths at *d/D* = 2 were all lower than those of the flat plate. As *d/D* increased, the average Nusselt numbers of *h/D* = 0.10 and 0.20 increased gradually, while that of *h/D* = 0.05 decreased. When *h/D* = 0.15, the average Nusselt numbers reached the maximum at *d/D* = 3; the maximum was 11.8% higher than that of the flat plate heat sink.

4. CONCLUSION

This work numerically investigated the flow and heat transfer characteristics of a liquid jet impinging on a cylindrical cavity heat sink with a local body heat source at different Reynolds numbers and cavity structures. The Transition SST turbulence model was validated and adopted. The main conclusions are as follows.
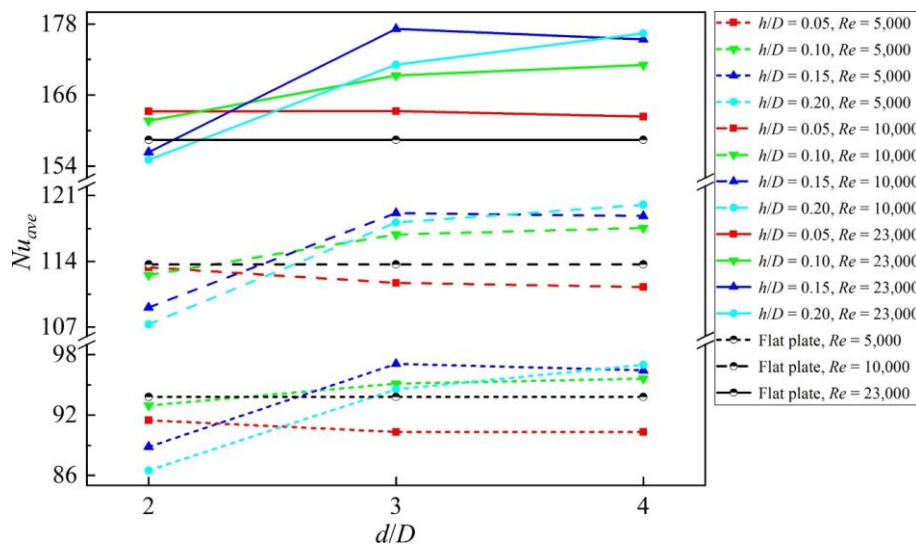

Fig. 11. Distributions of the average Nusselt numbers.

The cylindrical cavity structure can improve the heat transfer capacity of the heat sink. Compared to the flat plate heat sink, the maximum enhancement was found to be 11.8% when *d/D* = 3, *h/D* = 0.15, and *Re* = 23,000. However, the small-diameter (*d/D* = 2) and shallow-depth (*h/D* = 0.05) cylindrical cavity was found to not enhance the heat transfer performance, and even deteriorated it. Both had similar flow and heat transfer characteristics in the stagnation region due to their similar structures. The local Nusselt number of the cylindrical cavity heat sink near the sidewall area of the cavity was much lower than that of the flat plate heat sink. An inclined jet was observed after the fluid leapt out of the cavity, which introduced a horseshoe vortex. The average Nusselt number of the cylindrical cavity heat sink was found to be higher than that of the plate heat sink in most cases.

REFERENCES

Abouali, O. and N. Baghernezhad (2010). Numerical investigation of heat transfer enhancement in a microchannel with grooved surfaces. *Journal of Heat Transfer* 132, 41005-41013.

Baughn, J. W. and S. Shimizu (1989). Heat transfer measurements from a surface with uniform heat flux and an impinging jet. *ASME Journal of Heat Transfer* 111(4), 1096-1098.

Baughn, J. W., A. E. Hechanova and X. Yan (1991). An experimental study of entrainment effects on the heat transfer from a flat surface to a heated circular impinging jet. *ASME Journal of Heat Transfer* 113(4), 1023-1025.

Bhagwat, A. B. and A. Sridharan (2016). Numerical simulation of oblique air jet impingement on a heated flat plate. *Journal of Thermal Science and Engineering Applications* 9(1), 011017.

Buchlin, J. M. (2011). Convective heat transfer in impinging- gas-jet arrangements. *Journal of Applied Fluid Mechanics* 4(2), 137-149.

Chan, B. (2015). Heat transfer characteristics of aluminum foam heat sinks subject to an impinging jet under fixed pumping power. *International Journal of Heat Mass Transfer* 84 (5), 1056-1060.

Chandramohan, P., S. N. Murugesan and S. Arivazhagan (2016). Heat transfer analysis of flat plate subjected to multijet air impingement using principal component analysis and computational technique. *Journal of Applied Fluid Mechanics* 10(1), 293-306.

Elebiary, K. and M. E. Taslim (2011). Experimental/numerical crossover jet impingement in an airfoil leading-edge cooling channel. *ASME Turbo Expo: Turbine Technical Conference and Exposition* 135 (1), 1397-1409.

Fleischer, A. S. and S. R. Nejad (2004). Jet impingement cooling of a discretely heated portion of a protruding pedestal with a single round air jet. *Experimental Thermal and Fluid Science* 28(8), 893-901.

Huang, X., W. Yang, T. Ming, W. Shen and X. Yu (2017). Heat transfer enhancement on a microchannel heat sink with impinging jets and dimple. *International Journal of Heat and Mass Transfer* 112, 113-124.

Kumar, C. S. and A. Pattamatta (2017). Assessment of heat transfer enhancement using metallic porous foam configurations in laminar slot jet impingement: an experimental study. *Journal of Heat Transfer* 140(2), 022202.

Martin, H. (1977). Heat and mass transfer between impinging gas jets and solid surfaces. *Advanced Heat Transfer* 13, 1-60.

Robinson, A. J., R. Kempers, J. Colenbrander, N. Bushnell and R. Chen (2018). A single phase hybrid micro heat sink using impinging micro-jet arrays and microchannels. *Applied Thermal Engineering* 136, 408-418.

Shuja, S. Z., B. S. Yilbas and M. O. Budair (2005). Jet impingement onto a cylindrical cavity: consideration of annular nozzle cone angles, and cavity diameter. *International Journal of Computational Fluid Dynamics* 19(7), 483-492.

Shuja, S. Z., B. S. Yilbas and M. O. Budair (2007). Jet impingement on cylindrical cavity: Conical nozzle considerations. *Journal of Fluids and Structures* 23, 1106-1118.

Shuja, S. Z., B. S. Yilbas and S. Khan (2009). Jet impingement onto a conical cavity: Effects of annular nozzle outer angle and jet velocity on heat transfer and skin friction. *International Journal of Thermal Sciences* 48, 985-997.

Tang, Z. G., Q. Q. Liu, H. Li and X. T. Min (2017). Numerical simulation of heat transfer characteristics of jet impingement with a novel single cone heat sink. Applied Thermal Engineering 217, 906-914.

Terekhov, V. I., S. V. Kalinina, Y. M. Mshvidobadze and K. A. Sharov (2009). Impingement of an impact jet onto a spherical cavity. Flow structure and heat transfer. *International Journal of Heat and Mass Transfer* 52(11-12), 2498-2506.

Tuckerman, D. B. and R. W. Pease (1981). High-performance heat sinking for VLSI. *IEEE Electron Device Letters* 2(5), 126-129.

Wong, K. C. and S. Indran (2013). Impingement heat transfer of a plate fin heat sink with fillet profile. *International Journal of Heat Mass Transfer* 65(7), 1-9.

Xie, Y. H., P. Li, J. B. Lan and D. Zhang (2013). Flow and heat transfer characteristics of single jet impinging on dimpled surface. *Journal of Heat Transfer-Transactions of the ASME* 135(5), 052201.

Yan, X., J. W. Baughn and M. Mesbah (1992). The effect of Reynolds number on the heat transfer distribution from a flat plate to an impinging jet. *ASME Heat Transfer Div.* 226, 1-7.

Yang, L., J. Ren, H. Jiang and P. Ligrani (2014). Experimental and numerical investigation of unsteady impingement cooling within a blade leading edge passage. *International Journal of Heat and Mass Transfer* 71, 57-68.

Yilbas, B. S. and S. Z. Shuja (2009). Jet impingement onto a cylindrical cavity: Effect of jet velocity on heat transfer and skin friction. *International Journal of Numerical Methods for Heat & Fluid Flow* 19(2), 182-200.

Zhang, D., H. Qu, J. Lan, J. Chen and Y. H. Xie (2013). Flow and heat transfer characteristics of single jet impinging on protrusioned surface. *International Journal of Heat and Mass Transfer* 58(1-2), 18-28.

Zhao, J., S. Huang, L. Gong and Z. Huang (2016). Numerical study and optimizing on micro square pin-fin heat sink for electronic cooling. *Applied Thermal Engineering* 93, 1347-1359.